

Resonant carrier dynamics in biased superlattices in presence of dissipation

Pavel Abumov and D. W. L. Sprung

*Department of Physics and Astronomy, McMaster University
Hamilton, Ontario L8S 4M1 Canada*

(Dated: January 13, 2019)

We study electron dynamics in a biased undriven ideal semiconductor superlattice near energy level anticrossings, in the presence of dissipation due to homogeneous level broadening. In particular, we examine the dependence of wavepacket dynamical characteristics on electric field detuning, and investigate mixed regimes involving a superposition of energy level anticrossings showing both Rabi oscillations and resonant Zener tunneling. In recent work [Phys. Rev. B **75** 165421 (2007)], Rabi and Zener resonances were shown to have a common origin, and a criterion for the occurrence of either was proposed. The results obtained allow a better understanding of the nature of an interminiband resonance, which can be useful in the areas of microwave radiation generation and matter manipulation on the particle level.

PACS numbers: 73.23.-b, 73.21.Cd, 78.20.Bh, 78.30.Fs

I. INTRODUCTION

Carrier dynamics in a biased superlattice (SL) has remained an active topic during the last two decades. Knowledge of the underlying physical processes is necessary for a better understanding of perpendicular transport of carriers in multi-quantum well systems, as well as for successful development of applications, such as microwave radiation generation [1, 2, 3, 4], quantum computing [5, 6] and matter manipulation on the particle level [7].

Studies focused on coherent carrier dynamics revealed some dynamical features of great interest (see, for example, [8] and [9] and references therein). However, even more important aspects of resonant dynamics in a SL come from the interplay between coherent interminiband oscillations and incoherent tunneling to the continuum. This question goes back to the famous quantum-mechanical problem of tunneling in presence of dissipation [10, 11, 12] and has been considered for superlattices in [13]. Whereas typically such studies involve a number of approximations, we chose a computational approach with few limitations. This enabled us to consider resonant dynamics at high and moderate bias, specifically Rabi oscillations (RO) and resonant Zener tunneling (RZT), and to establish a relation between these two fundamental types of interminiband transport. In the first place, it helps in understanding the damping mechanism of RO and to propose ways to reduce it. It also provides a link between RO and RZT, an instance where quantum transport theory has been lacking to date. These results can be applied to any system possessing a Wannier-Stark ladder structure, e.g. photonic crystals [14].

II. RESONANT INTERMINIBAND DYNAMICS

This work focusses on longitudinal motion of a single electron in a zero-temperature biased superlattice. Our approach involves solutions $\Psi(x, t)$ of the time-dependent

Schrödinger equation (TDSE) in a biassed periodic potential

$$V(x) = \sum_{n=-\infty}^{\infty} V_{SL}(x - nd) + xF, \quad \text{where}$$
$$V_{SL}(x) = \frac{V_0}{2} \left[\tanh \frac{x + a/2}{\sigma} - \tanh \frac{x - a/2}{\sigma} \right] \times \Theta(x) \Theta(d - x). \quad (1)$$

where $\Theta(x)$ is the Heaviside function vanishing for $x < 0$. $F = -eE$ is a uniform bias, E the electric field, and $V_{SL}(x)$ is the model potential in a unit cell of width d , and barrier thickness a of the periodic system. Parameters of several GaAs/Ga_{1-x}Al_xAs layered heterostructures considered are shown in Table I. Our numerical solutions of Eq. 1 used discrete transparent boundary conditions [9, 15], to make the domain finite.

The norm of the quasibound part of the wavepacket ρ and miniband occupancy ρ_ν provide a convenient means to monitor interminiband dynamics; miniband occupancy means the wavepacket projection onto a tight-binding miniband ν : $\rho_\nu = \sum_k |\langle \Psi(x, t) | W_\nu^k(x) \rangle|^2$. Here $W_\nu^k(x)$ stands for a Wannier-Stark (WS) quasibound state corresponding to energy level E_ν^k centered on the well with index k , and belonging to miniband ν ($\nu=1,2, \dots$); the initial wavepacket is centered on the well with index 0. The tight-binding Wannier functions from miniband ν are denoted as $w_\nu(x)$.

We will consider several different superlattices labelled $X = A, B, C, D$ in Table I. To refer to an interminiband resonance originating from an anticrossing of energy levels E_ν^k and E_μ^{k+n} in biased sample X , we will use the symbol $\mathcal{R}_{\nu\mu}^n(X)$ and we will denote the resonant bias (the value of bias at which the peak of a resonance is observed) as F_n , n being the resonance index ($n = 1, 2, \dots$). When of little importance, some indices may be omitted for brevity. For convenience the symbol G will stand for inverse bias $1/F$ ($G_n = 1/F_n$). Unless specified otherwise, time is measured in units of the Bloch period $T_B = 2\pi\hbar/Fd$.

Name	V_0 , meV	d , nm(ML)	a , nm(ML)	σ , nm
Sample A	212	13.0 (46)	3.1 (11)	0.4
Sample B	250	17.3 (61)	2.5 (9)	0.4
Sample C	212	13.0 (46)	2.3 (8)	0.4
Sample D	212	13.0 (46)	2.5 (9)	0.4

TABLE I: Geometric parameters of the model potentials used in simulations. Barrier height of 212 meV corresponds to $x=0.18$ and of 250 meV to $x=0.3$ in the GaAs/Ga_{1-x}Al_xAs structure; ML stands for monolayer thickness, 1 ML = 0.283 nm.

A. Rabi oscillations model

Typically, Rabi Oscillations (RO) are a result of interminiband transitions under external radiation when its frequency approaches the inherent system's value $\omega_{12} = (E_2 - E_1)/\hbar$ [16]. This pumping provides excitation of carriers and their subsequent spontaneous emission, which is widely used in quantum cascade lasers [17]. A comprehensive overview of RO in the two-miniband approximation has been given by Ferreira and Bastard [18] and further mathematical details can be found in references [19, 20, 21]. In a biased SL, interminiband transitions may also occur in the absence of external radiation [22, 23, 24]: when energy levels from coupled Wannier-Stark ladders (WSL) align in neighbouring wells, a carrier can easily tunnel between them while undergoing non-radiative transitions.

For an undriven SL (i.e. not exposed to an external oscillating electric field) a fruitful analogy can be made to the well-understood system of a two-level atom under external monochromatic radiation $V(t) = E_0 \hat{\mu} \cos(\omega t)$, where $\hat{\mu} = x$ is the dipole transition operator between adjacent minibands MB1 and MB2, and E_0 is the amplitude of the external electric field. Let us take the WS states to be stationary and orthogonal, assuming very large carrier lifetime $1/\Gamma$ compared to a typical RO period for moderate bias. With that, the acceleration theorem $\hbar(d\vec{k}/dt) = \vec{F}$, combined with the dispersion relation

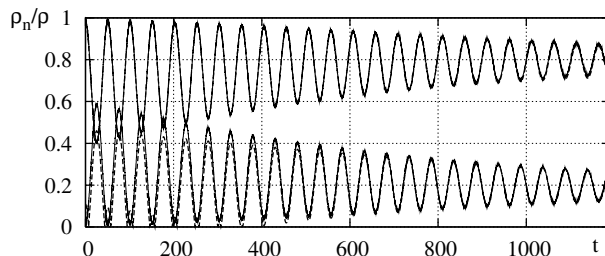


FIG. 1: Occupancy functions (solid lines) and their fit from Eq. 6 (broken lines) for $\Psi(x,0) = w_1(x)$ near resonance $\mathcal{R}_{12}^3(\mathbf{A})$ at $G = 0.44058$ nm/meV (0.8 HWHM away from the resonant bias); the upper curve corresponds to $n = 1$ and the lower to $n = 2$.

can describe wavepacket evolution over a Bloch oscillation cycle, by using the decomposition $V(x) = V_{SL} + Fx$:

$$\langle x(t) \rangle = \frac{1}{\hbar} \int_0^t \frac{dE(k_0 + Ft/\hbar)}{dk} dt \quad (2)$$

In the case of tightly bound lowest minibands which is common for a semiconductor SL, carrier dispersion in MB n can be approximated as $E(k) = E_n + (\delta E/2) \cos(kd + n\pi)$ and the mean position evolves as $\langle x(t) \rangle = (L/2)(\cos(\omega_B t) - 1)$ for $F > 0$, where ω_B is the Bloch angular frequency and L is the Bloch Oscillation (BO) domain width. If the real-space origin is placed at $\langle x(t) \rangle$, the wavepacket's evolution in space at fixed energy can heuristically be replaced by its evolution in kinetic energy space, while retaining a fixed mean real-space position. The effective potential in MB n then becomes $V_n(x, t) = V_{SL}(x) + \frac{\delta E_n}{2} \cos(\omega_B t + n\pi)$ which looks much like the potential of an irradiated atom: the system has a natural frequency $\omega_{12} = (E_2 - E_1)/\hbar$ and is effectively driven at the Bloch frequency. The Schrödinger equation for such a system at resonance field F_n becomes

$$-i\hbar \frac{\partial \Psi(x, t)}{\partial t} = (\hat{H}_0 + \hat{V}) \Psi(x, t) \quad (3)$$

with $\hat{V} = \hat{x} F_n \cos(\omega_B t)$,

where \hat{H}_0 refers to an undriven biased SL in the tight-binding approximation. An expression for the population of the second level with initial wavepacket $\Psi(x, 0) = W_1(x)$ can be now obtained in the same fashion as for an atom-like system [16]. Simple calculations show that in our case

$$\omega_{12} - \omega \equiv \omega_{12} - n\omega_B = \frac{(E_1 - E_2)^2}{n d \hbar} (G_n - G)$$

is the difference between the system's frequency at the n^{th} resonance, and the driving BO frequency. With necessary modifications, for a two-level system driven off its ground state we obtain

$$\frac{\rho_2}{\rho}(t) = \left(\frac{\rho_2}{\rho}\right)^{\text{max}} \mathcal{L}(G) \sin^2 \frac{\pi t}{T_R^{\text{max}} \sqrt{\mathcal{L}(G)}} \quad (4)$$

$$\frac{\rho_1}{\rho}(t) = 1 - \frac{\rho_2}{\rho}(t), \quad \text{with}$$

$$\mathcal{L}(G) \equiv \left[1 + \left(\frac{G - G_n}{\Gamma}\right)^2\right]^{-1} \quad \text{where} \quad (5)$$

$$\Gamma = x_{0n}/(E_2 - E_1),$$

$$T_R^{\text{max}} = d/x_{0n},$$

$$x_{nm} = \langle W_1^n(x) | x | W_2^m(x) \rangle,$$

where n is the index of the resonance considered. These equations are straightforwardly generalized to an arbitrary pair of interacting minibands. Note that in order to predict the $\rho_2/\rho(t)$ curve in the entire near-resonance

region we only require values of the dipole matrix element x_{nm} and of $(\rho_2/\rho)^{max}$ computed at the resonant bias field. In this simplistic derivation for a two-level tightly bound system, we have neglected dispersion of the wavepacket in the process of BO, nevertheless it can give a quite satisfactory explanation, as will be seen below.

We first consider moderate fields, where the BO domain is typically smaller than a potential cell width; that implies that: (i) energy levels are sparse due to large splitting of WSL; hence near a resonance there is one preferred tunneling path between MB1 and MB2; (ii) at a resonance, WS states are reasonably localized and have an exponentially vanishing tail, so we expect that $x_{0n} \propto e^{-n}$ (this has been predicted by a two-level model for an atom [23] and also has been explicitly calculated for a driven multiband SL [25]).

The above derivations were made for system in a steady state. However, in practice an initial non-equilibrium configuration undergoes a relaxation process. To study this we could take a linear combination $\Psi(x, t = 0) = c_1 w_1(x) + c_2 w_2(x)$ of tight-binding Wannier states as the initial wavefunction. (Obtaining correct quasibound WS functions is a significant task in itself [25, 26] and is not important for our primary goal to study steady-state RO dynamics.) The mechanisms underlying the tunneling process do not depend on the particular linear combination: components of $\Psi(x)$ which belong to higher minibands tunnel out rapidly during the initial relaxation period, which only scales down the norm of the quasibound wavepacket being observed in a steady mode. The coefficients c_1 and c_2 should be set so that after an initial period of relaxation of a non-equilibrium state, the resulting RO are clear and of sufficient magnitude. The maximum of RO magnitude reaches nearly unity for the two extreme cases $|c_1| = 1$ and $|c_2| = 1$, with less carrier decay for the former choice. Hence, it is sufficient to take the initial wavefunction to be $\Psi(x, t = 0) = w_1(x)$ to obtain useful results.

B. Near-resonance parameter behavior

By studying isolated Rabi resonances, it has been found [9] that a carrier undergoing RO produces damped oscillations in miniband occupancy, of the form:

$$\rho_n/\rho(t) = P_n + A_R e^{-\gamma_A t} \cos\left(\frac{2\pi t}{T_R} + \phi_n\right),$$

$$\text{with } \rho(t) = \exp\left(-\gamma t - \sigma(1 - e^{-\gamma_{ne} t})\right) \quad (6)$$

in agreement with the general theory [27]. Here T_R , A_R and γ_A are the period, amplitude and decay rate of Rabi oscillations respectively; ϕ_n is an initial phase determined by a particular form of $\Psi(x, 0)$ (e.g. $\phi_1 \approx 0$ for $\Psi(x, 0) = w_1(x)$); γ is the decay rate of the entire wavepacket and P_n is asymptotic value of $\rho_n/\rho(t)$ in the limit $t \rightarrow \infty$. The term $-\sigma(1 - e^{-\gamma_{ne} t})$ represents a

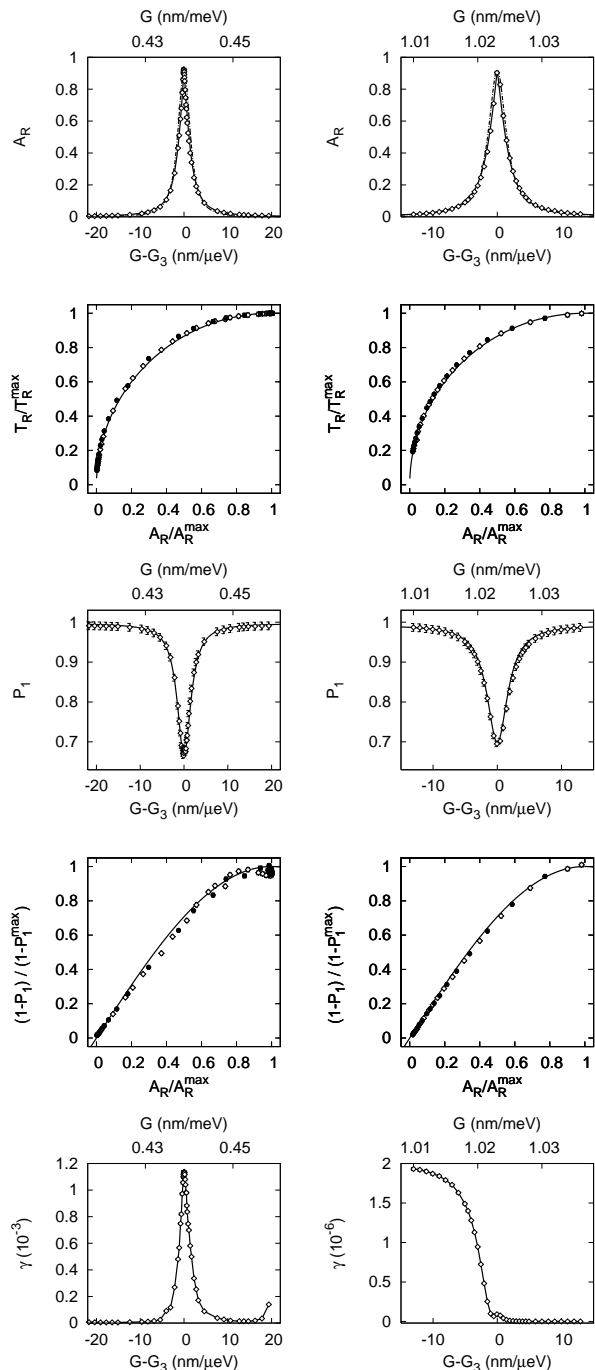


FIG. 2: Behavior of key dynamical parameters for $\mathcal{R}_{12}^3(\mathbf{A})$ (left column) and $\mathcal{R}_{12}^3(\mathbf{B})$ (right column). Top panel shows RO amplitude vs. inverse bias (chain-dotted line shows a Lorentzian fit $\mathcal{L}(G)$, solid line shows fit from Eq. 9), second from top panel: relative RO amplitude vs. relative RO period (filled circles correspond to $G < G_3$, empty circles to $G > G_3$; solid line shows fit from Eq. 9 given Eq. 7), third from top panel: asymptotic occupancy of the first miniband vs. inverse bias (solid line shows fit from Eq. 9), fourth from top panel: relative RO period vs. asymptotic occupancy of the first miniband (filled circles correspond to $G < G_3$, empty circles to $G > G_3$; solid line shows fit from Eq. 9); bottom panel: carrier decay rate vs. inverse bias.

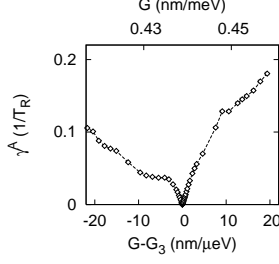


FIG. 3: Damping rate of RO vs. inverse bias for $\mathcal{R}_{12}^3(\mathbf{A})$ in units of $1/T_R$.

dip in the decay rate due to two-exponential decay [28] and was found to be vanishingly small close to the resonant bias. Its presence is due to the initial relaxation of wavepacket components orthogonal to eigenfunctions of the current miniband, with σ being proportional to the norm of the orthogonal part and γ_{ne} being the relaxation rate, typically larger by two orders of magnitude than γ . A typical example of time evolution of near-resonant interminiband occupancy dynamics, and its fit from Eq. 6 is shown in Fig. 1.

Since the parameters in Eq. 6 provide a good description of carrier dynamics, we focus on examining their behaviour around a resonance. As was shown previously [9], the period T_R of Rabi oscillations shows a Lorentzian-like peak around the resonant bias:

$$T_R(G) = T_R^{max} \sqrt{\mathcal{L}(G)}, \quad (7)$$

with \mathcal{L} defined in Eq. 6. We will refer to the Lorentzian parameter Γ as the HWHM (half-width at half-maximum) of the resonance under consideration.

For a double quantum well system, perturbation theory predicts that the frequency of Rabi oscillations strictly at resonant bias is given by $\hbar\omega_R/2 = \langle \Psi_L | V(x) | \Psi_R \rangle$, the tunneling matrix element through the barrier separating the two wells [27] and is essentially the splitting between the energy levels. Thus the inverse of T_R^{max} of Eq. 7 is the minimum energy level splitting at their anticrossing.

As derived from the simulation results, the parameters A_R and P_n have clear extrema as well. The following equations fit the data quite well (Fig. 2):

$$A_R = A_R^{max} \left[1 - \sqrt{1 - \mathcal{L}_{\nu\mu}^n(G)} \right], \quad (8)$$

$$\tilde{P}_n = \tilde{P}_n^{max} \sin \frac{\pi A_R}{2A_R^{max}},$$

with A_R^{max} and \tilde{P}_n^{max} being the peak values; $\tilde{P}_n = P_n$ for the lower resonantly coupled MB and $1 - P_n$ for the upper one. The other two parameters, γ and γ_A , are extremely sensitive to coupling to higher minibands and their bias

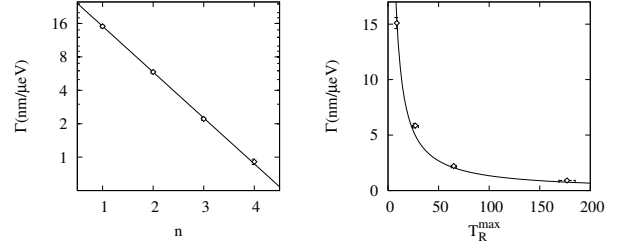


FIG. 4: Logarithmic fit of Γ_n versus resonance index for $\mathcal{R}_{12}^3(\mathbf{A})$ (left) and its relation to T_R^{max} (right).

detuning dependence varies from one resonance to another. However, at a resonant bias γ_A always reached its virtually zero minimum, and γ its maximum (Fig. 2, 3).

As the index n rises, $\mathcal{R}_{\mu\nu}^n$ are expected to become narrower, since the length of the tunneling pathway into the adjacent miniband increases and so does the system's sensitivity to bias detuning, due to related frequency detuning of the Bloch oscillations; this is reflected in a decrease of x_{0n} in Eq. 6. We have shown previously [9] that the peak period of Rabi oscillations changes exponentially with resonance index n :

$$T_n^{max} = T_1^{max} \left(T_2^{max} / T_1^{max} \right)^{n-1}.$$

As predicted by Eq. 6, the resonance HWHM dependence on n closely follows an exponential law (Fig. 4) as well:

$$\Gamma_n = \Gamma_1 \left(\Gamma_2 / \Gamma_1 \right)^{n-1} \quad (9)$$

The anticipated relation

$$T_n^{max} = G_0 / \Gamma_n \quad (10)$$

also holds quite well: fitting Eq. (9) produced a value $T_n^{max} \Gamma_n = (139 \pm 5)$ nm/ μ eV compared to $G_0 = (145 \pm 1)$ nm/ μ eV for sample A, and calculations for sample B showed that

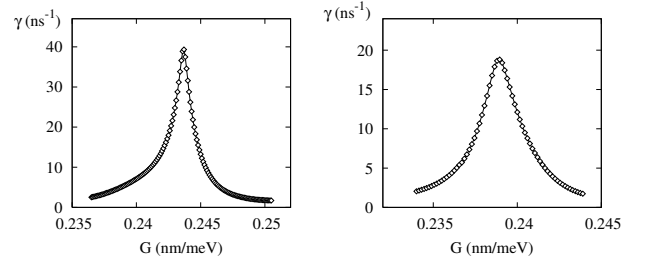


FIG. 5: Decay rate γ of a wavepacket vs. inverse bias, near $\mathcal{R}_{13}^5(\mathbf{C})$ (left) and $\mathcal{R}_{13}^6(\mathbf{D})$ (right).

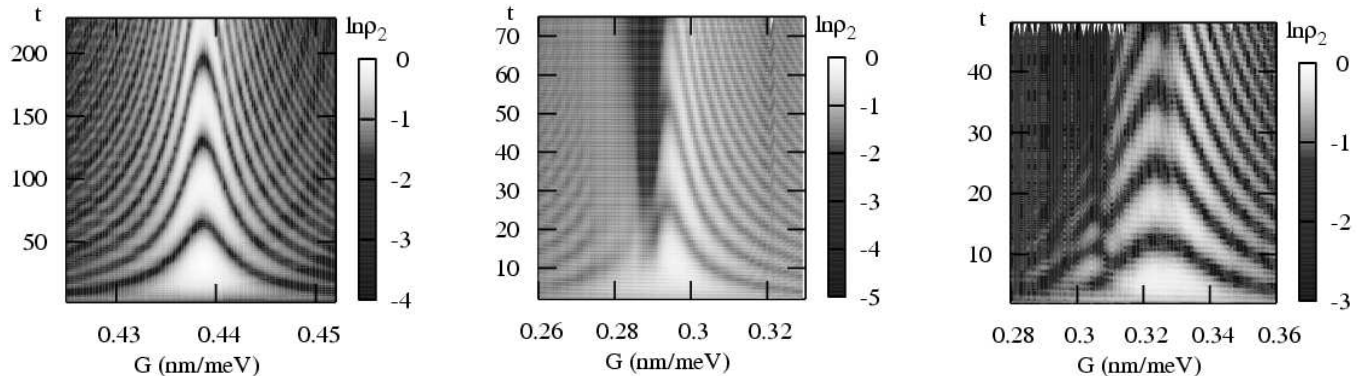


FIG. 6: Near-resonant dynamics of second miniband occupancy at \mathcal{R}_{12}^3 (A) (left), \mathcal{R}_{12}^3 (C) (center) and \mathcal{R}_{12}^2 (B) (right).

$T_3^{max}\Gamma_3 = (1.05 \pm 0.01)$ nm/meV compared to $G_0 = (1.02 \pm 0.01)$ nm/meV.

When an ensemble of resonantly coupled minibands is weakly bound, resonant Zener tunneling (RZT) [29, 30, 31] prevails over RO; we will call these Zener resonances. In this case the carrier excitation decays very quickly and does not exhibit persistent RO. Then γ becomes the key parameter in the dynamical description and features a clear peak centered about the resonant bias (Fig. 5). Sensitivity of γ to coupling to higher minibands makes the shape of curves $\gamma(G)$ differ for different resonances.

III. RABI OSCILLATIONS AND RESONANT ZENER TUNNELING

In section IIB we have been considering isolated inter-miniband resonances; typically, they occur in a strong potential at moderate fields where resonances have narrow HWHM compared to their spacing in inverse bias space and hence they rarely overlap. In a more realistic example of a high-field resonance in a weaker potential, the in-

teraction between just two resonantly coupled minibands represents only one of many interference paths. For moderate potentials, such as $\text{Al}_{0.3}\text{Ga}_{0.7}\text{As}$, incoherent coupling to higher minibands has strong enough influence on overall dynamics and one can observe mixed regimes exhibiting overlapping Zener and Rabi resonances that simultaneously cause resonant Zener tunneling and Rabi oscillations.

A. Superposition of resonances

We now consider a case of overlapping Rabi and Zener resonances, to illustrate how coherent and incoherent dynamics interfere at a near-resonant bias. This typically occurs when the HWHM of a Rabi resonance is large compared to the HWHM of a Zener resonance, since the latter requires coupling to the higher minibands. Then one resonance is seen to be superimposed on another, as in the center panel of Fig. 6. At the \mathcal{R}_{13}^5 peak, RO vanish and the $P_1(G)$ and $A_R(G)$ curves demonstrate a sharp extremum resembling a superposition of two Lorentzian-

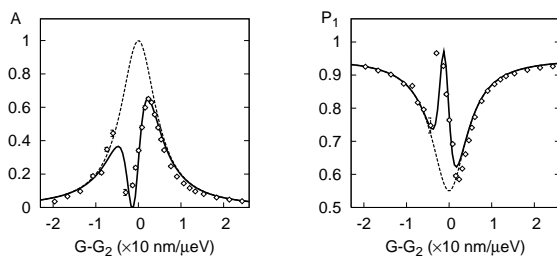


FIG. 7: Amplitude of RO and of first miniband occupancy near resonances \mathcal{R}_{12}^2 and \mathcal{R}_{13}^5 from middle panel of Fig. 6. Solid lines show a superposition of Lorentzian curves best fitting simulation data, in circles; broken line is an estimate of a fit in the absence of \mathcal{R}_{13}^5 .

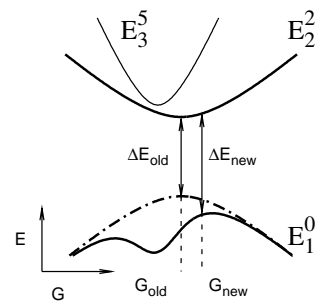


FIG. 8: Schematics showing mutual impact of energy levels anticrossings. Chain-dotted line shows position of level E_1^0 in the absence of repulsion from level E_3^5 , shown as a thin solid line.

like curves (Fig. 7).

Fig. 6 represents a few typical cases of interminiband resonances arrangement. The leftmost panel is an example of an isolated Rabi resonance having a close to perfectly symmetric structure; the two panels to the right are examples of interference between Rabi and Zener resonances. In the middle panel, the Zener resonance \mathcal{R}_{13}^5 appears to be particularly strong and dominating. Hence, to the right of the Rabi resonance \mathcal{R}_{12}^2 peak, one can clearly see an oscillatory pattern, whereas to the left of the peak it is smeared out by incoherent Zener tunneling. The close presence of the Zener resonance \mathcal{R}_{13}^5 has also the effect of shifting the Rabi resonance \mathcal{R}_{12}^2 peak along the bias scale.

From the relation $F_n = n F_0$, the resonance \mathcal{R}_{12}^2 (center panel of Fig. 6) should have a peak at $G = (0.284 \pm 0.002)$ nm/meV; however as the maximum period of oscillations indicates, it is located at a lower bias $G = (0.295 \pm 0.002)$ nm/meV. The shift occurs because at the energy level anticrossing corresponding to \mathcal{R}_{13}^5 , the levels E_0^1 and E_3^5 are repelled from each other [25]. At the same time, the position of level E_2^2 involved in a Rabi resonance remains almost unchanged. Provided that the minimum mismatch of coupled energy levels ($E_2^2 - E_0^1$) produces the longest period of RO [9], this results in a shift of the Rabi resonance \mathcal{R}_{12}^2 peak as demonstrated in Fig. 8. There the minimum energy difference at \mathcal{R}_{12}^2 , ΔE_{old} , located at G_{old} in the absence of a \mathcal{R}_{13}^5 anticrossing, shifts to G_{new} due to superposition of the energy level anticrossings \mathcal{R}_{12}^2 and \mathcal{R}_{13}^5 . Since the repulsion from the two anticrossings adds constructively, ΔE_{old} is larger than ΔE_{new} , and since the RO period is inversely proportional to the mismatch in energy level alignment, the peak period of RO shifts to a new value of bias. Thus the proximity of another resonance has a twofold effect on the resonance considered: it shifts its resonant bias and reduces the maximum period of RO. The latter effect is demonstrated in the rightmost panel of Fig. 6, where a weak and narrow Zener resonance spread over $G = 0.322 \dots 0.330$ nm/meV reduces the RO period.

B. Conditions for Rabi resonance

The issue of RO persistence leads in the direction of separating coherent from incoherent dynamics. The simulation data reveal that a slower decay of RO occurs far from Zener resonances and in stronger potentials, with strongly bound lowest minibands reducing the carrier decay rate γ . At the same time, the RO decay rate nearly vanishes at the very peak of a Rabi resonance, where the wavepacket tunneling rate is at its highest. Thus the tunneling rate by itself is not a reliable indicator of Rabi oscillation damping. Fig. 9 demonstrates Zener tunneling and Rabi oscillation patterns at the same tunneling rate, observed for bias values F_2 and F_3 , respectively.

In the center panel of Fig. 6 at inverse bias $G^{(3)} = 0.312$ nm/meV there is a clear RO pattern, whereas

at the bias $G^{(1)} = 0.274$ nm/meV which is symmetric to $G^{(3)}$ about the Rabi peak (located at $G = 0.293$ nm/meV), Rabi oscillations die out quickly. This behavior does not agree with the previously found [9] symmetric structure of an isolated resonance (left panel of Fig. 6); it is interference of a Zener resonance at $G^{(1)}$ that overdamps the Rabi oscillations. To generalize, the alignment of energy levels from higher minibands sets the wavepacket behavior model and the link between RO and RZT (that are both a product of wavepacket self-interference) is determined by a particular arrangement of Wannier-Stark ladders: specifically, by the ratio of interminiband tunneling rates, as will be shown below.

For illustrative purposes, let us turn again to the two-miniband model and denote the rate of tunneling from $MB\nu$ to $MB\mu$ as $\gamma_{\nu\mu}$; this is a convenient measure of strength of interminiband coupling. The magnitude of $\gamma_{\nu\mu}$ is inversely proportional to the difference in energy between the resonantly coupled energy levels from $WSL\nu$ and $WSL\mu$ [32]. In case of middle panel of Fig. 6, these level pairs are: E_1^0 and E_2^2 for the Rabi resonance and E_1^1 and E_3^5 for the Zener resonance. For the inverse biases $G^{(2)}$ and $G^{(3)}$ featuring the same carrier decay rate (as seen in Fig. 9), the difference $(E_2^2 - E_1^0) - \Delta E_{21}$ determining the tunneling between MB1 and MB2 is -2 meV and 6.2 meV, correspondingly (ΔE_{21} is the energy spacing between the centers of MB2 and MB1 which equals 88.8 meV for potential A), whereas at the same values of bias, $(E_3^5 - E_1^1) - \Delta E_{31}$ for the ensemble of MB1 and MB3 equals -10 meV and 10 meV. Considering that the widths of the tight-binding MB1, MB2 and MB3 are 8.8, 39.4 and 98.6 meV, the disparity between the two values of $(E_2^2 - E_1^0) - \Delta E_{21} \propto 1/\gamma_{12}$ is much more significant than that of $(E_3^5 - E_1^1) - \Delta E_{31} \propto 1/\gamma_{13}$. Hence, the ratio γ_{12}/γ_{23} , which shows the strength of isolation of the coupled bands MB1 and MB2, from higher minibands, is much smaller in the case of $G^{(1)}$. Due to a weaker isolation of the ensemble at $G^{(1)}$, the quasibound oscillating

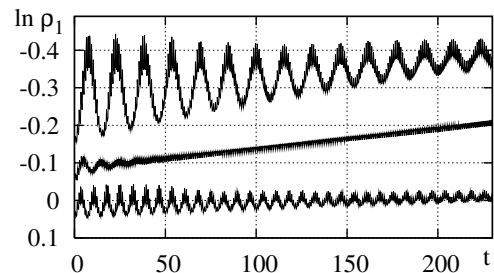


FIG. 9: Dynamics of first miniband occupancy in the vicinity of \mathcal{R}_{12}^2 , from the center panel of Fig. 6 at $G^{(3)} = 0.301$ nm/meV (upper curve), $G^{(2)} = 0.293$ nm/meV (middle curve) and $G^{(1)} = 0.274$ nm/meV (lower curve). The upper [lower] curve is shifted upwards [downwards] by 0.1 for visibility.

C. RO damping and quantum interference

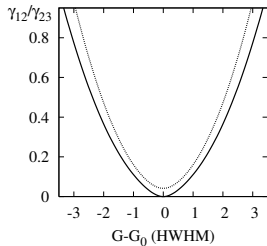


FIG. 10: Ratio of interminiband tunneling rates γ_{12}/γ_{23} vs. inverse bias (in resonance HWHM units), from Eq. 11 given Eq. 9. Solid and broken lines show the cases when $P_1 = 0.5$ and 0.6 at resonance (ideal and nearly ideal cases), correspondingly.

part of the wavepacket is more subject to incoherent tunneling into the continuum, so RO are destroyed and turn more quickly into RZT which is demonstrated in Fig. 9.

This also explains why, at the peak of an isolated Rabi resonance, the RO damping rate is the lowest. For example, at R_{12} two lowest minibands merge through resonant coupling, so γ_{12} and γ are exploding while γ_{23} changes relatively little. Thus, a peaking ratio of γ_{12}/γ_{23} makes RO decay go nearly to zero at the peak, despite homogeneous level broadening which reaches its greatest extent there. Away from the peak γ falls off and RO persistence decreases, because of the quick drop in γ_{12} (Fig. 3). This is a somewhat counterintuitive example of how a quasi-bound state with shorter lifetime can be more coherent.

Since γ_{12} is closely related to the interminiband transition matrix element V_{12} , we can estimate the near-resonant behavior of the latter by invoking some dynamic equilibrium considerations. From elementary two-miniband model calculations (see Appendix A) we get

$$\frac{\gamma_{12}}{\gamma_{23}} = \frac{2P_1 - 1}{P_1(1 - P_1)} \quad (11)$$

Neglecting tunneling pathways between poorly aligned energy levels (e.g. $E_1^0 \rightarrow E_2^1$ at \mathcal{R}_{12}^2) and over many potential wells (in case of resonance across three minibands), $V_{12} = \gamma_{12}$. Assuming that γ_{23} changes over bias near \mathcal{R}_{12} adiabatically slowly compared to γ_{12} , we get $V_{12} \propto \frac{(2P_1 - 1)}{P_1(1 - P_1)}$; with the fit for $P_1(G)$ from Eq. 9, we can estimate the behavior of V_{12} as shown in Fig. 10. In the ideal case of $P_1 = 0.5$ at the peak, γ_{12} vanishes, which reflects a complete merger of the two lowest minibands. This example shows a link between the data obtained for bias detuning dependencies of the key dynamical parameters, and theoretical values. With few simplifying approximations, one can investigate near-resonant behavior of theoretical values based on carrier dynamics in a superlattice system in the above manner, using described system of coupled damped oscillators [33].

RO damping originates from self-interference of a wavepacket that is facilitated by interference between small bits of wavefunction that a wavepacket constantly emits through intrawell and Bloch oscillations (here denoted ‘ripples’). A wavepacket initially set in the ground miniband of a biased SL, starts to leak out into the second miniband, since the interference of the ‘ripples’ is constructive at the location of the initially unpopulated MB2, and destructive at MB1. When most of the wavepacket has tunneled out into MB2, the tunneling direction reverses. This follows since by then most of the emission is from MB2. In the ideal case of zero RO damping, this reversion is a mirror process; in practice, the tunneling rate to higher minibands cannot be neglected. This causes the amount of emitted ‘ripples’ to reduce faster in MB2; such an inequality breaks the mirror symmetry of the two transitions. The oscillation pattern smears out and RO are damped more quickly, the larger is the imbalance in the rate of ‘ripples’ escaping to the continuum. That is, inversely proportional to γ_{12}/γ_{23} . In other words, if γ_{23} cannot be neglected compared to γ_{12} , it breaks the anisotropy in the system’s tunneling pathways: in addition to $MB1 \leftrightarrow MB2$, there appear two additional pathways, $MB1 \leftrightarrow MB3$ and $MB2 \leftrightarrow MB3$ with very different tunneling rates.

IV. CONCLUSION

From the results of numerical simulations of near-resonant carrier dynamics at an isolated resonance, we have proposed a set of equations governing wavepacket behavior; the dynamical parameters near a resonance were found to exhibit extrema of various shapes. For overlapping resonances, a superposition of energy level anticrossings produces a shift in resonant bias. It also reduces the maximum period of RO and perturbs the dependence of dynamical parameters on bias. A superposition of Rabi and Zener resonances also allowed us to observe the transition between coherent and incoherent wavepacket dynamics, and to examine the mechanism of RO damping.

Persistence of Rabi oscillations near a resonance was demonstrated to be independent of homogeneous level broadening and to depend on the ratio of interminiband tunneling rates γ_{12}/γ_{23} , which can serve as a quantitative prediction of the RO damping rate.

Acknowledgments

We are grateful to NSERC Canada for continuing support under discovery grant RGPIN-3198. We also thank Dr. W. van Dijk for his help with the numerical algorithm implementation. The numerical simulations were

carried out on the Shared Hierarchical Academic Research Computing Network (www.sharcnet.ca).

APPENDIX A: DYNAMIC EQUILIBRIUM FOR A TWO-MINIBAND SYSTEM

We consider an elementary system of two strongly interacting minibands coupled to continuum states. Further, let us denote the tunneling rate from $MB\nu$ to $MB\mu$ as $\gamma_{\nu\mu}$, from $MB\nu$ to continuum as $\gamma_{\nu\infty}$ and the current occupancy of $MB\nu$ as $\rho_\nu/\rho \equiv \tilde{\rho}_\nu$. In steady tunneling mode, the miniband occupancies are in dynamic equilibrium. Neglecting direct tunneling from MB1 to the continuum, the flow of probability is balanced as follows:

$$\begin{cases} \frac{d}{dt} \vec{\rho} = \begin{pmatrix} \gamma_{12} & -\gamma_{21} - \gamma_{2\infty} \\ -\gamma_{12} & \gamma_{21} \end{pmatrix} \vec{\rho} \\ \frac{d}{dt} \frac{\tilde{\rho}_1}{\rho_1 + \rho_2} = -\frac{d}{dt} \frac{\tilde{\rho}_2}{\rho_1 + \rho_2} \end{cases}$$

where $\vec{\rho}$ has components $\tilde{\rho}_1, \tilde{\rho}_2$, and the second equation expresses the condition for dynamic equilibrium. A little algebra takes us to the quadratic equation

$$\kappa^2 \gamma_{12} - \kappa(\gamma_{21} - \gamma_{12} + \gamma_{2\infty}) - \gamma_{21} = 0$$

with $\kappa = \tilde{\rho}_1/\tilde{\rho}_2 > 1$. Taking $\tilde{\rho}_2 = 1 - \tilde{\rho}_1$ and assuming $\gamma_{12} \approx \gamma_{21} = \gamma$ (which holds well in the vicinity of a resonance peak), in the steady-state limit $t \rightarrow \infty$ we arrive at

$$\alpha = \frac{2P_1 - 1}{P_1(1 - P_1)}$$

with the notation $\alpha = \gamma_{\infty}/2\gamma$ and $\gamma_{\infty} = \gamma_{2\infty}$. Note that the extreme case of RZT corresponds to $\alpha \rightarrow \infty$ with $P_1 \rightarrow 1$ and of RO to $\alpha \rightarrow 0$ with $P_1 \rightarrow 0.5$.

-
- [1] C. Waschke, H. G. Roskos, K. Leo, H. Kurz, and K. Köhler, *Semicond. Sci. Technol.* **9**, 416 (1994).
- [2] K. Jin, M. Odnoblyudov, Y. Shimada, K. Hirakawa, and K. A. Chao, *Phys. Rev. B* **68**, 153315 (2003).
- [3] Y. A. Romanov and Y. Y. Romanova, *Semiconductors* **39**, 147 (2005).
- [4] Y. Shimada, N. Sekine, and K. Hirakawa, *Appl. Phys. Lett.* **84**, 580 (2004).
- [5] A. Zrenner, E. Beham, S. Stuffer, F. Findeis, M. Bichler, and G. Abstreiter, *Nature* **418**, 612 (2002).
- [6] Q. Q. Wang, A. Muller, P. Bianucci, E. Rossi, Q. K. Xue, T. Takagahara, C. Piermarocchi, A. H. MacDonald, and C. K. Shih, *Phys. Rev. B* **72**, 035306 (2005).
- [7] B. M. Breid, D. Witthaut, and H. J. Korsch, *New J. Phys.* **9**, 62 (2007).
- [8] A. Latge, F. J. Ribeiro, A. Bruno-Alfonso, L. E. Oliveira, and H. S. Brandi, *Braz. J. Phys.* **36**, 898 (2006).
- [9] P. Abumov and D. W. L. Sprung, *Phys. Rev. B* **75**, 165421 (2007).
- [10] J. Shah, *Ultrafast spectroscopy of semiconductors and semiconductor nanostructures* (Springer-Verlag, Berlin and Heidelberg GM, 1999).
- [11] E. Beham, A. Zrenner, S. Stuffer, F. Findeis, M. Bichler, and G. Abstreiter, *Physica E* **16**, 59 (2003).
- [12] A. Vasanelli, R. Ferreira, and G. Bastard, *Phys. Rev. Lett.* **89**, 216804 (2002).
- [13] P. Han, K. J. Jin, Y. L. Zhou, Q. L. Zhou, H. B. Lu, D. Y. Guan, and G. Z. Yang, *Europhys. Lett.* **72**, 1011 (2005).
- [14] P. B. Wilkinson, *Phys. Rev. E* **65**, 056616 (2002).
- [15] C. A. Moyer, *Am. J. Phys.* **72**, 352 (2004).
- [16] V. M. Akulin and V. V. Karlov, *Coherent Interaction* (Springer-Verlag, Berlin, 1992).
- [17] F. J. Capasso, D. L. Sivco, C. Sirtori, A. L. Hutchinson, and A. Y. Cho, *Science* **264**, 553 (1994).
- [18] R. Ferreira and G. Bastard, *Rep. Prog. Phys.* **60**, 345 (1997).
- [19] H. S. Brandi, A. Latgé, Z. Barticevic, and L. E. Oliveira, *Sol. State Comm.* **135**, 386 (2005).
- [20] J. Rotvig, A.-P. Jauho, and H. Smith, *Phys. Rev. Lett.* **74**, 1831 (1994).
- [21] M. Glück, M. Hankel, A. R. Kolovsky, and H. J. Korsch, *J. Optics B* **2**, 612 (2000).
- [22] R. Ferreira, G. Bastard, and P. Voisin, *Solid-State Electronics* **37**, 857 (1994).
- [23] G. Bastard, R. Ferreira, S. Chelles, and P. Voisin, *Phys. Rev. B* **50**, 4445 (1994).
- [24] J. Bleuse, G. Bastard, and P. Voisin, *Phys. Rev. Lett.* **60**, 220 (1987).
- [25] M. Glück, A. R. Kolovsky, and H. J. Korsch, *Phys. Rep.* **366**, 103 (2002).
- [26] M. Glück, A. R. Kolovsky, H. J. Korsch, and F. Zimmer, *Phys. Rev. B* **65**, 115302 (2002).
- [27] F. A. Vasko and A. V. Kuznetsov, *Electronic states and Optical Transitions in Semiconductor Heterostructures* (Springer, New York, 1999).
- [28] S. A. Gurvitz and M. S. Marinov, *Phys. Rev. A* **40**, 2166 (1989).
- [29] S. Glutsch, *Phys. Rev. B* **69**, 235317 (2004).
- [30] A. Vojvodic, A. Blom, Z. S. Ma, Y. Shimada, K. Hirakawa, and K. A. Chao, *Sol. State Comm.* **136**, 580 (2005).
- [31] V. V. Konotop, P. G. Kevrekidis, and M. Salerno, *Phys. Rev. A* **72**, 023611 (2005).
- [32] G. Cohen, S. A. Gurvitz, I. Bar-Joseph, B. Devaux, P. Bergman, and A. Regreny, *Phys. Rev. B* **47**, 16012 (1993).
- [33] K. Leo, J. Shah, J. P. Gordon, T. C. Damen, D. A. B. Miller, C. W. Tu, and J. E. Cunningham, *Phys. Rev. B* **42**, 7065 (1990).